Dynamics of antisolvent processed hybrid metal halide perovskites studied by *in situ* photoluminescence and its influence on optoelectronic properties

*Tze-Bin Song1, Zhenghao Yuan1, Finn Babbe2, David P. Nenon3,4, Erkan Aydin5, Stefaan De Wolf5, Carolin M. Sutter-Fella1**

1 Chemical Sciences Division, Lawrence Berkeley National Laboratory, Berkeley, CA 94720, US

2 Joint Center for Artificial Photosynthesis, Lawrence Berkeley National Laboratory, Berkeley, CA 94720, USA

3 Department of Chemistry, University of California, Berkeley, Berkeley, California 94720, United States

4 Material Sciences Division, Lawrence Berkeley National Laboratory, Berkeley, California 94720, United States

5 King Abdullah University of Science and Technology (KAUST), Thuwal 23955-6900, Kingdom of Saudi Arabia

ORCHID
Tze-Bin Song: 0000-0002-1645-9831
Finn Babbe: 0000-0002-9131-638X
David P. Nenon: 0000-0002-2045-5219
Erkan Aydin: 0000-0002-8849-2788
Stefaan De Wolf: 0000-0003-1619-9061
Carolin Sutter-Fella: 0000-0002-7769-0869

Corresponding Author

*E-mail:
Carolin M. Sutter-Fella: csutterfella@lbl.gov

Abstract

The antisolvent dripping time during spin-coating of $CH_3NH_3PbI_3$ ($MAPbI_3$) strongly impacts film morphology as well as possible formation of the intermediate precursor phase, and – consequently – device performance. Here, we use *in situ* photoluminescence (PL) to directly monitor the fast-occurring changes during $MAPbI_3$ synthesis. These measurements reveal how the ideal timing of the antisolvent leads to homogeneous nucleation and pinhole-free films. In addition, these films show significantly reduced nonradiative recombination with 1.5 orders of magnitude difference in absolute PL quantum yield compared to films where no antisolvent is applied. Low-temperature PL measurements confirm that antisolvent treatment reduces the number of trap states presumably in the bulk material. However, if the antisolvent is dripped late, heterogeneous nucleation via the orthorhombic $(MA)_2(DMF)_2Pb_3I_8$ intermediate phase leads to a needle-like morphology that can be correlated to a red-shifted *in situ* PL signature. We find that the ideal dripping window is very narrow when using dimethylformamide as the solvent, confirmed by device performance metrics. Finally, the use of *in situ* PL is discussed to gain information on nucleation, growth and ultimately increase reproducibility.

Keywords: halide perovskites, solution synthesis, antisolvent, in situ characterization, nucleation, recombination.

ToC

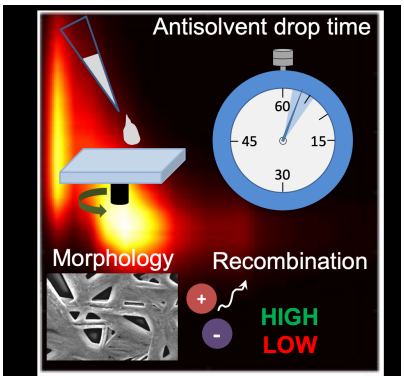

Introduction

The family of hybrid metal halide perovskites generally described by the ABX_3 structure (with A = MA (methylammonium), FA (formamidinium), Cs or other alkali metals; B = Pb, Sn, and X = I, Br, Cl) has sparked enormous research activities in the last decade given their plentiful photo-physical peculiarities,[1–4] unprecedented optoelectronic device performance enhancements,[5] and ease of fabrication.[6–8] To date, the most employed techniques are based on chemical solution processing making use of spin-coating or print-/blade-coating deposition.[9–13]

The conventional recipe to form $MAPbI_3$ employs stoichiometric molar ratios of MAI and PbI_2 or over stoichiometric molar ratios of MAI:PbX_2 (X = Cl, I, or acetate) precursors.[14,15] However, the photovoltaic power conversion efficiency (PCE) of early devices was limited by poor surface coverage and poor crystalline morphology typically encountered in one-step solution-deposited films.[16,17] Both, coverage and morphology, critically depend on the formation of intermediate phases.[18–21] An important step forward was the dripping of an antisolvent onto the wet precursor film during the perovskite spin-coating process in order to induce crystallization leading to smooth and pinhole-free films. This antisolvent process was described by their pioneers as ‘fast crystallization deposition’ or application of a ‘non-dissolving solvent’.[13,22] Antisolvents which improve film formation often exhibit low polarity and dielectric constants, high boiling points,

good miscibility with the precursor solvent, and cannot dissolve any perovskite or related precursor phase.[8,23,24] The most commonly used antisolvents are toluene[13], chlorobenzene[22], and diethyl ether,[24] but many others have been tested as well.[21,22,24–26] The aim of the antisolvent is to accelerate the crystallization process, induce homogeneous nucleation with high nucleation density, thus promote uniform grain growth leading to significantly improved morphology, surface coverage, and formation of larger grains.[18,21,27–29] This is achieved by the antisolvent via washing out the solvent, thus creating an oversaturated solution leading to perovskite growth.[27] Concerning the antisolvent treatment, many factors including the nature of the antisolvent, the antisolvent temperature as well as the antisolvent drip time are critical for the final sample quality as it influences the solution solvent-antisolvent interaction. The antisolvent treatment does not only influence the morphology, surface roughness, and crystallinity but also affects the optical and electronic properties of the perovskite film and consequently device performance.[8,27–31] The optimum time window to drip the antisolvent is small, often in the seconds range (depending on the exact chemistry and solvents used), with the boundaries being set by solvent evaporation rate and formation of intermediate phases.[18]

Although antisolvent-assisted deposition is the most popular synthesis approach yielding PCEs consistently > 20%,[7] fundamental insight with regard to the dynamic phase transition and influence on optoelectronic properties is missing. Recent studies using *in situ* X-ray diffraction revealed that the antisolvent has to be dripped before intermediate phases start to crystallize and that the chemical complexity of the perovskite film leads to a widening of the processing window.[18,32] However, few studies provide direct *in situ* mechanistic insights on the influence of the antisolvent timing on nucleation, densification, and growth. In this work, we synthesize $MAPbI_3$ films using chlorobenzene as the antisolvent. We aim at providing a holistic picture of

the antisolvent drip time by using *in situ* photoluminescence measurements to monitor the fast-occurring changes during synthesis. We study the influence of the antisolvent drip time on morphology, crystal phase formation, optoelectronic film quality, and device performance. It is demonstrated how *in situ* photoluminescence emission can be used to characterize nucleation and growth phenomena. We found that the dripping of the antisolvent interferes with the crystallization pathway, avoiding intermediate phase formation if the antisolvent is dripped at the right time leading to the formation of smooth and pinhole-free films with reduced nonradiative recombination pathways and reduction of trap states. Our study enables insights into nucleation, densification and growth and how the timing of the antisolvent interacts with these fundamental processes using laboratory-based *in situ* photoluminescence measurements. PLQY measurements on $MAPbI_3$ with different film morphology provide evidence that the antisolvent treatment reduces nonradiative recombination channels possibly by reducing the probability of bulk defect formation. From a device perspective, the ideal dripping window is small using DMF as a solvent, leading to significant losses in short-circuit current and fill factor if the antisolvent is dripped too early or late.

Result and discussions

$MAPbI_3$ films were synthesized on glass substrates by spin-coating and antisolvent (chlorobenzene) dripping, followed by annealing at 100 ºC (details on the synthesis can be found in the Experimental section). Here, the antisolvent drip time *X* is the time when the antisolvent is dispersed after the second spin cycle has started *i.e.* 500 rpm for 5s is followed by 4,000 rpm for 60s and the antisolvent is dripped *X*s into the 4,000 rpm spin cycle. Note, that the antisolvent drip time, even if the same process/recipe is used, can vary from operator to operator; therefore, we do not aim at highlighting an exact optimum time but rather consequences of early/ideal/late

dripping of the antisolvent. First, in Figures 1a-d (and Supporting Information S1) we compare the morphology for different antisolvent drip times to a reference sample synthesized without antisolvent after 10 min of annealing. The scanning electron microscopy (SEM) images show the formation of a compact, pinhole-free film only if the antisolvent is dripped at an optimum time which is 5s in this study. If the antisolvent is dripped earlier the film contains pinholes (3s, Figure 1a), and if it is dripped later, it exhibits the needle-like structure (7s, Figure 1c), similar as in the film without antisolvent (Figure 1d). Accordingly, the visual appearance of the film changes from specular to diffuse reflection (insets in Figure 1a-d). A possible reason for the encountered morphology if the antisolvent is dripped early is that the wet film is too thick and the precursor solution is far away from supersaturation.[22] In order to better understand the morphological appearance, X-ray diffraction (XRD) measurements were performed to characterize crystal phases and film crystallinity after application of different antisolvent drip times as well as the effect of annealing time (no annealing, 10 and 20 min annealing in Figures 1e-h). All diffraction patterns confirm the formation of tetragonal $MAPbI_3$ phase even without annealing.[33,34] Co-presence of PbI_2 (diffraction peak ~12.7º) and intermediate orthorhombic phase $(MA)_2(DMF)_2Pb_3I_8$ was observed when the antisolvent was dripped late, as well as in the film without antisolvent.[19,35] In a previous study we performed *in situ* diffraction and optical microscope measurements during the synthesis of $MAPbI_3$ and confirmed the formation of the intermediate $(MA)_2(DMF)_2Pb_3I_8$ phase together with the needle-like morphology.[35] In addition, enabled by a fully remotely controlled spin coater in the synchrotron hutch, we found that this phase does not require thermal activation but forms already during spin coating and converts into the perovskite phase after about 15s of annealing.[35] Thus, if the antisolvent is dripped late (or in the absence of an antisolvent) PbI_2-MAI-DMF[36] (N,N-dimethylformamide) complex formation

happens which templates the final film structure into a non-compact, needle-like morphology.[18,19,35] Upon annealing, the crystallinity significantly improves, as evidenced by the drop in full width at half maximum (FWHM) of the (110) peak (~14.1º) (Supporting Information Figure S2). The smallest FWHM characteristic for larger domain sizes is observed if the antisolvent is dripped late or no antisolvent is applied. This observation can be explained by the fact that the dripping of the antisolvent accelerates precipitation and crystallization from a high nucleation density leading to smaller crystal domains. Based on those results, the critical time window to drip chlorobenzene under our experimental conditions is < 4s. However, solvent and mixed solvents influence the precursor phase formation as well as the *ideal* antisolvent dripping window. Therefore, each process will require its specific optimization process.

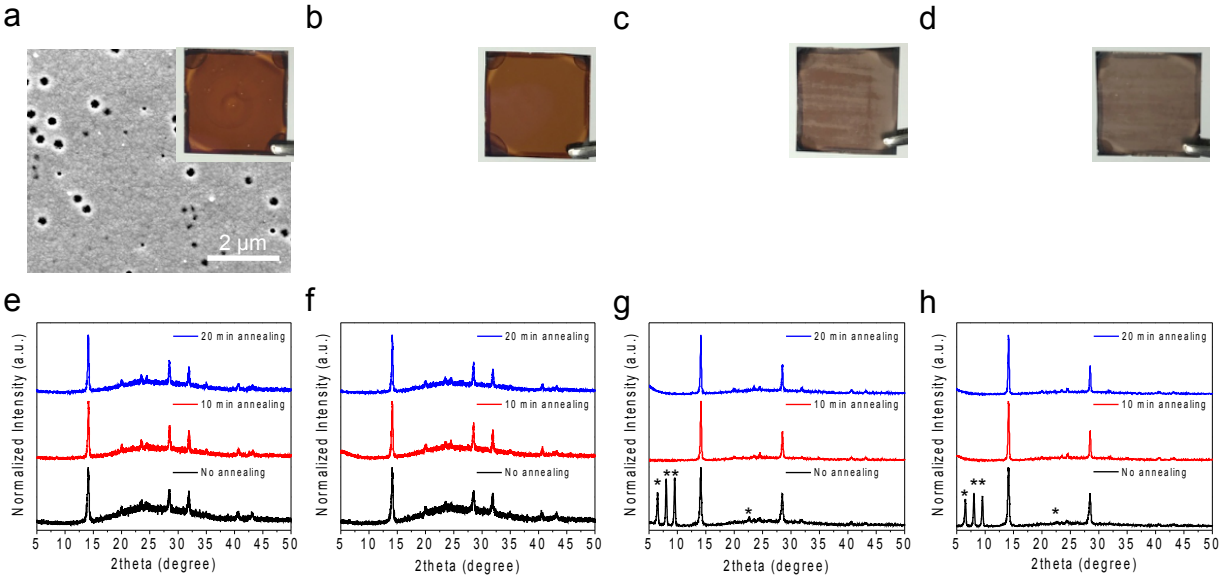

Figure 1. SEM images of $MAPbI_3$ films were the antisolvent was dripped after a) 3s, b) 5s, c) 7s, and d) without antisolvent, respectively (total of 10 min annealing at 100 ºC). Insets illustrate pictures of the films. e-h) Diffraction patterns of $MAPbI_3$ films were the antisolvent was dripped after 3s, 5s, 7s, and without antisolvent, respectively (total of 0-20 min annealing at 100 ºC). * is used to indicate $(MA)_2(DMF)_2Pb_3I_8$ phase.

Next, *in situ* photoluminescence (PL) measurements were taken during the thermal annealing on the hot plate at 100 ºC, immediately following the spin-coating process (Figure 2 and Supporting Information S3). Several characteristics can be seen and will be discussed first, before correlating these findings with the antisolvent drip time and its implication on material properties. In Fig. 2a and 2b, the PL emission is centered around ~1.63 eV and exhibits one intensity maximum (Fig. 2 e,f). In Fig. 2c and 2d, the PL emission gradually shifts from high (~1.8 eV) to low energy (~1.63 eV) resulting in $\Delta E = 160$ meV and shows two intensity maxima (Fig. 2g,h). Finally, the emission intensity eventually drops by more than one order of magnitude over time for all samples. In a first approximation, the energy of the spectral maximum can be interpreted as the bandgap of the material.[37] A shift in emission energy correlated to crystallite size has been found by others before.[38–40] In these studies, the magnitude of the redshifted ΔE was up to 25 meV and thus, considerably smaller than what we find here. In contrast, Akkerman *et al.* synthesized perovskite nanoplatelets using colloidal synthesis and found a ΔE of about 150 meV.[41] Although, the chemistry of colloidal synthesis is different, we propose that nanometer-scale nucleation precedes the growth of $MAPbI_3$ films and we interpret the high energy emission as quantum-confined nucleation. This finding aligns with a proposed nano-assembly model proposed for the formation of $MAPbI_3$ films.[42] It is reportedly excluded that the high energy emission stems from the $(MA)_2(DMF)_2Pb_3I_8$ phase confirmed by *in situ* PL measurements taken during spin coating.[35] Next, we discuss the PL intensity change. The PL emission spectrum exhibits two intensity maxima in Fig. 2c and 2d. Based on the previous discussion, two effects could contribute to the PL intensity change with the first signal being dominated by nucleation and densification and the second signal, which is centered at the actual bandgap of bulk $MAPbI_3$ (~1.6 eV at room temperature, here ~1.63 eV at 100 ºC), reflects crystal growth. The overall

intensity decrease over time is probably caused by photodarkening and thermally induced effects.

With the scope of different antisolvent drip times, *in situ* PL measurements are particularly powerful because the PL evolution is very distinct if the antisolvent is dripped late, showing a large ΔE and two intensity maxima. This PL signature could indicate heterogeneous, nanoscale nucleation and growth, instead of homogeneous nucleation and growth if the antisolvent would have been dripped before 6s. The SEM top-view images confirm a narrower crystal size distribution in the latter case. *In situ* PL measurements clearly illustrate in real-time how the antisolvent treatment forces nucleation of the halide perovskite phase, as evidenced by PL emission at ~1.63 eV (very small ΔE) and the diffraction data. Furthermore, it can be seen that the antisolvent accelerates perovskite formation, as expected. These results illustrate that insight provided by *in situ* PL is very useful to fine-tune synthesis conditions and could provide a means to improve reproducibility.

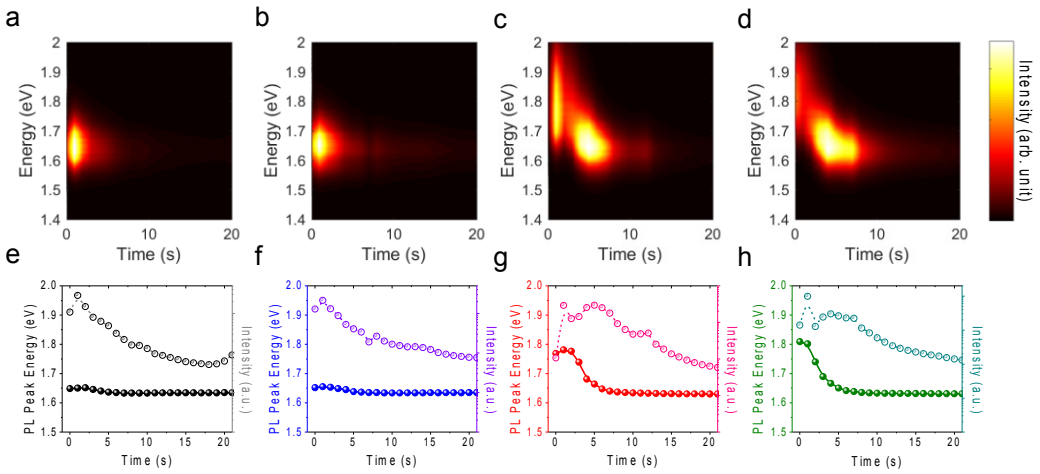

Figure 2. a-d) *In situ* PL contour plot of $MAPbI_3$ films taken on the hot plate after dripping the antisolvent after 3s, 5s, 7s, and without antisolvent, respectively. e-h) Corresponding PL peak position and intensity.

In order to investigate how the antisolvent drip time influences optoelectronic properties, we performed quantitative and temperature-dependent PL measurements (Figures 3 and S4). Figure 3a shows the absolute PL quantum yield (PLQY) for antisolvent drip time. Generally, PLQY measurements provide insights into the prevalence of nonradiative recombination losses.[3,43,44] Without antisolvent, the PLQY is 1.5 orders of magnitude lower than for films synthesized with antisolvent. Given that film morphology without antisolvent is similar to the morphology when the antisolvent was dripped late (compare Figure 1c+d), we attribute the low PLQY to a high number of nonradiative decay pathways due to the presence of defects. These results indicate that the application of the antisolvent at the optimum time decreases the presence of nonradiative decay pathways in the final material. Similarly, the ideal timing of the antisolvent dripping can improve film quality apparent by a relatively higher PLQY for shorter dripping times. Intermediate formation of $(MA)_2(DMF)_2Pb_3I_8$ (Figure 1g+h) as compared to fast and direct formation of $MAPbI_3$ could also influence final film quality. A higher defect density if formation proceeds via the intermediate phase cannot be ruled out. The PLQY can be directly related to an optically implied open-circuit voltage (V_{oc}) defined as .[45,46] The implied V_{oc} is 1.12 V if no antisolvent is applied and 1.21, 1.21, and 1.20 V if the antisolvent is applied after 3, 5, and 7s, respectively, assuming a bandgap of 1.65 eV (Figure 3a). The implied V_{oc}'s present an upper boundary for the achievable V_{oc} based on the intrinsic material quality of the absorber film, disregarding potential losses at hetero interfaces and contacts.[3,47]

Next, we performed low-temperature PL measurements at 80K (Figure 3b and SI Figure S4). $MAPbI_3$ undergoes a crystal phase change from tetragonal to orthorhombic at around 150K which is accompanied by a bandgap increase.[34,48] PL spectra in Fig. 3b shows several features:

emission from the tetragonal (TP) and orthorhombic (OP) phases centered ~791 nm and ~748 nm, respectively, and a very broad defect emission band towards higher wavelengths ($\lambda > 810$ nm). Emission from the OP varies for the different samples, and emission from the TP dominates. Previously, spatially inhomogeneous phase transition and an incomplete phase transition upon cooling were explained by strain.[49,50] Given the different sample morphologies (Fig. 1a-d), it is likely that there is a variation in strain level. Wu *et al*. reported similar low-temperature PL spectra for $MAPbI_3$ grown with PbI_2 precursors that exhibit a broad defect emission.[51] The appearance of the broad shoulder confirms the presence of defects in all samples and thus, explains losses in PLQY. The breadth of the high wavelength shoulder confirms an increased concentration of defects if no antisolvent is applied or dripped late and the least defect emission when the antisolvent was dripped within 5s. The PLQY data taken at room temperature showed the highest PL yield when the antisolvent was dripped at 3s. Although low-temperature PL and room temperature PLQY measurements are related, there is not necessarily a causal connection because here, the PLQY measured by an integrating sphere setup is a combination of band-edge emission and defect emission.

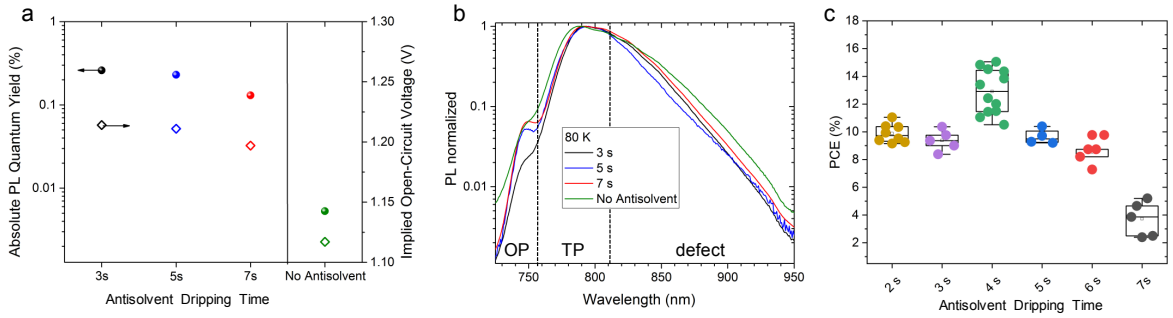

Figure 3. a) Absolute PL Quantum Yield and extracted implied open-circuit voltage versus antisolvent dripping time. b) PL spectra of $MAPbI_3$ samples with and without antisolvent treatment taken at 80 K. OP and TP indicate emission corresponding to orthorhombic and tetragonal phase, respectively. c) The power conversion efficiency of photovoltaic devices from two independent batches exhibiting the highest performance at 4s drip time.

Finally, we investigate the antisolvent drip time (1 - 7s) on photovoltaic device performance using a *p-i-n* structure with glass/ITO/NiO_x/$MAPbI_3$/PCBM/BCP/Ag architecture (details are given in the Experimental Section) to confirm the narrow antisolvent dripping window using DMF solvent. Figure S5 (Supporting Information) shows a picture of the devices with antisolvent drip times between 1 - 7s as well as SEM top-view images for 2, 4, and 7s. The same morphology as described in the first part is observed for $MAPbI_3$ films deposited with different antisolvent drip times on NiO_x films. Highly consistent trends and device statistics from two individual batches have been found for the different antisolvent drip times as summarized in Figure 3c and S6 (Supporting Information). The data confirm the highest PCEs to occur at an optimized drip time of 4s. The device V_{oc} is the least impacted parameter and only drips significantly for 2 and 7s. This drip can be related to the completely different morphology observed at 2 and 7s. Although, the PCBM has been reported to act as a passivation molecule via accepting an electron from the PbI_3^- antisite defects or under-coordinated halide ions,[52] the difference of ~ 170 mV between the implied V_{oc} and the electrical V_{oc} indicates losses at the $MAPbI_3$/contact interfaces. The J_{sc} highly depends on the antisolvent drip time with reduced J_{sc} once needle-like morphology emerges. The Fill Factor (FF) is consistently lower outside the optimum condition due to increased shunt resistance (Figure S7, Supporting Information). Given the device statistics, changes are clearly observable and reproducible.

We showed that the antisolvent dripping time, which is the time when the interaction of the solution solvent with the antisolvent starts, does not only influence morphology but also

optoelectronic properties which can be correlated to solar cell device performance (summarized in Figure 4). The antisolvent dripping can be divided into three stages, in agreement with the findings by Xiao *et al*.[22] In stage I, the antisolvent is dripped early when the wet film is thick, and the solution is not close to saturation resulting in films with pinholes. In stage II (ideal), the wet film thickness has reduced and the precursor concentration is high, possibly at the stage of supersaturation, and there is still sufficient solvent remaining to aid rearrangement leading to pinhole-free film formation. During stage I and II, the intermediate phase does not form before the antisolvent is dripped. *In situ* PL suggests homogeneous nucleation as confirmed by a small crystal size distribution (top view SEM) and fast crystallization. In stage III (late), crystallization started before the antisolvent was dripped (same as if no antisolvent is dripped). Diffraction measurements showed a larger domain size for stage III samples where nucleation probably proceeds heterogeneously with lower nucleation density than in stages I and II (indicated by *in situ* PL measurements). Samples of stage III proceed via the formation of intermediate phase ($(MA)_2(DMF)_2Pb_3I_8$) alongside perovskite formation before thermal annealing. The presence of this intermediate phase templates morphology. *In situ* PL allows for the direct monitoring of nucleation and growth and displays a distinct signature, which is a red-shift in PL emission if the antisolvent is dripped late. This information can be used for process optimization and control. The PLQY is significantly lower if no antisolvent is applied. This low PLQY can be explained by the presence of nonradiative recombination pathways caused by defects. Considering recombination to happen preferentially at surfaces/grain boundaries or in the bulk, we hypothesize that if an antisolvent treatment is applied, the probability of bulk defect formation is reduced. This hypothesis is based on the observation that film morphology is the same with similar surface area in stage III where the antisolvent is dripped late or no antisolvent is dripped

at all, but significant difference in PLQY (1.5 orders of magnitude). Possibly, this interaction of the antisolvent happens at the molecular level which would explain why the antisolvent drip time is so important considering the fast changes in the molecular precursor during the first few seconds during spin coating. Devices synthesized with different antisolvent drip times confirm a very narrow window for best performance.

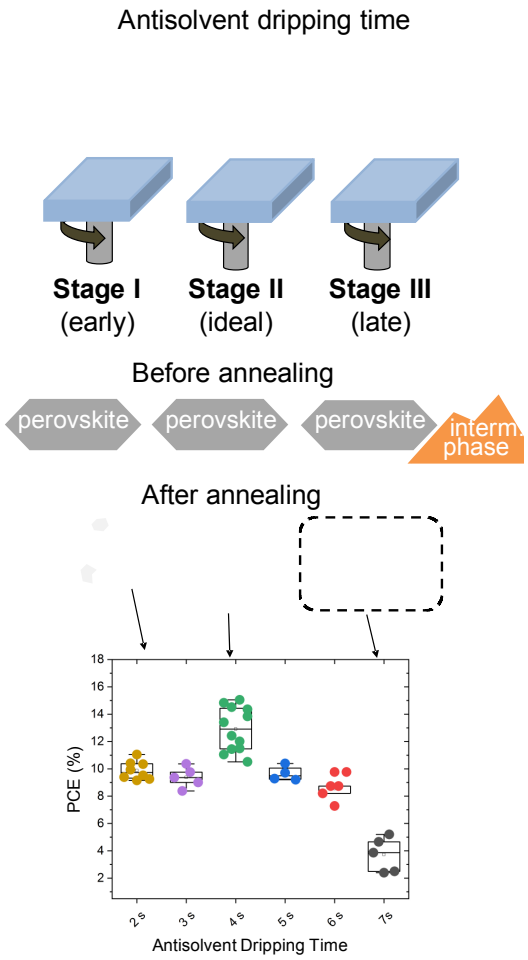

Figure 4. Overview of the effect of the antisolvent dripping time divided into three stages and its direct effect on morphology, co-existence of intermediate phase, as well as photovoltaic power conversion efficiency.

Conclusion

In summary, we have investigated the effect of the antisolvent dripping time on the morphology, crystallinity, and optoelectronic properties of $MAPbI_3$ thin films and devices. Morphology critically depends on the *ideal* dripping time; otherwise, pinholes or the typical needle-like morphology appear if the antisolvent is dripped early or late, respectively. The appearance of pinholes can be explained by a too thick wet film layer far away from supersaturation, while the formation of the needle-like morphology can be correlated to the intermediate orthorhombic $(MA)_2(DMF)_2Pb_3I_8$ phase confirmed by XRD. This intermediate phase dictates final film morphology. *In situ* PL measurements during annealing of $MAPbI_3$ samples informs nucleation and growth kinetics. If the antisolvent is applied late or not at all, a redshift in PL is observed during the annealing step, a redshift in PL suggests quantum-confined growth starting with very small nuclei and broad PL emission, indicating heterogeneous nucleation. This redshift is very small otherwise because the growth happened even before annealing. PLQY measurements provide evidence that antisolvent treatment reduces nonradiative recombination channels irrespective of film morphology possibly by reducing the likelihood of bulk defect formation which is happening at the molecular level during antisolvent-solvent interaction. Finally, photovoltaic devices metrics illustrate the small ideal dripping window with significant losses in J_{sc} and FF if the antisolvent is dripped too early or late. Our results demonstrate that precise control of the antisolvent process will provide homogeneous pinhole-free morphology, manipulate the phase formation pathway, and leads to better optoelectronic properties and optimized device performance.

Experimental Section

Film fabrication. Methylammonium iodide (CH_3NH_3I, MAI) (Greatcell Solar) and anhydrous N,N-dimethylformamide (DMF, 99.8%) were purchased from Sigma-Aldrich. Lead iodide (PbI_2, 99.9985%) was purchased from Alfa Aesar. Chlorobenzene was purchased from Acros Organics (extra dry, 99.5%). Chemicals were used as received. The precursor solutions to form $MAPbI_3$ films were prepared following the originally most frequently used preparation recipes.[6,15,53] We used molar ratios of 0.6 M MAI to 0.6 M PbI_2 (ratio 1:1). All precursors were dissolved in DMF. $MAPbI_3$ films were prepared on glass substrates by spin coating process at 500 rpm for 5 s followed by 4,000 rpm for 60 s in the glovebox using 50 µl of the precursor solution. After spin coating, the films were annealed at 100 °C on a hotplate in the glovebox for 0 - 20 min. 300 µl chlorobenzene was dripped during the fast-spinning step at the time indicated.

Photoluminescence. *In situ* PL measurements were acquired on a home build setup using a 532 nm laser diode, a plano-convex lens above the substrate, a 550 nm long-pass filter and a fiber coupled Ocean Optics spectrometer (Flame). A maximum power density of ~30 mW/cm^2 was used during *in situ* PL measurements on glass substrates. PL emission signals were fitted using single Gaussian peak fitting after linear background removal, R^2 >0.998.

Low temperature PL measurements were acquired on a home build setup with excitation from a collimated 532 nm diode laser source, with the photoluminescence signal captured through a 50x Olympus objective (0.1 or 1s acquisition per spectrum), 550 nm long-pass filter and a plano-convex lens focused onto the fiber leading to the Ocean Optics QE Pro Spectrometer. For the temperature dependent measurements, samples mounted on a cold finger in a vacuum chamber cooled with liquid nitrogen. Low temperature heat-transfer compound was

applied to the samples to facilitate thermal equilibrium in vacuum. PL spectra were measured from 80 K to 380 K, with 20 K increments at the same spot and the same excitation density. At each temperature, the sample was allowed to thermally equilibrate for 10 minutes before the PL measurement was taken. A maximum power density of ~800 mW/cm^2 was used during the temperature dependent PL measurements (80 K to 300 K and slightly higher power density for measurements > 300 K). $MAPbI_3$ films were annealed for 10 min.

Absolute PL quantum yields were determined optically using a home-built integrating sphere spectrofluorometer. The planar thin-film samples were oriented to avoid direct reflections back out of the entry port and prevent totally internally reflected light from leaving directly through the exit port, as these would yield incorrect PLQY values. A bare glass slide with the same orientation served as a blank. A pulsed single wavelength laser (Power Technology LDCU 12/6692) emitting at 440 nm was used for the PLQY measurements with an excitation power of 9.7 mW over ~1 mm^2. PLQY values were calculated by integrating the counts of the $MAPbI_3$ thin film emission then comparing that value to the absorbed light at 440 nm. More details can be found in the Supporting Information and a complete description of this home-built integrating sphere spectrofluorometer can be found elsewhere.[54] $MAPbI_3$ films were annealed for 10 min.

Device fabrication. The perovskite solar cells have been fabricated in p-i-n configuration. For this, we first deposited 25 nm of NiO_x films that were deposited on the pre-cleaned ITO substrates (XinYan Technologies, 15 ohm/sq) via RF magnetron sputtering as defined previously.[55] On top, $MAPbI_3$ perovskite films were deposited as defined above with the precursor solution being 1.25 M for device fabrication instead of 0.6 M. The antisolvent quenching time was varied as defined in the main text. Next, a 20 mg/ml solution of $PC_{60}BM$ (>99.5%, Solenne BV) in chlorobenzene was spin-coated onto the perovskite films at 3000 rpm

for 30 seconds. Finally, an ultra-thin layer of bathocuproine (Sigma Aldrich) was spin-coated at 6000 rpm for 30 seconds from a 0.5 mg/ml solution in anhydrous ethanol. Devices were completed by the thermal evaporation of a 100 nm thick silver contact at 10^{-6} Torr.

The devices were tested under standard 1-sun illumination (100 mW/cm^2, AM 1.5G, 25 °C) using Abet Technologies Sun 3000 Solar Simulator equipped with Autolab Potentiostat/Galvanostat. The measurements were performed in a glove box. The light intensity was calibrated using a calibrated reference cell (RERA Solutions, calibrated at Radboud University Nijmegen). Perovskite solar cells tested at a 200 mV/s scan rate. Devices had a 0.1 cm^2 square active area as can be seen in Figure S5a. Note that reverse scan is from V_{oc} to J_{sc} (forward bias → short circuit, 1.2 V → -0.1V), and forward scan is from J_{sc} to V_{oc} (short circuit → forward bias, -0.1 V → 1.2 V). No preconditioning protocol has been used before the measurement.

Other Material Characterizations. A field emission scanning electron microscopy (SEM, Quanta FEG 250, FEI) was used to acquire SEM images. An electron beam acceleration of 5 kV was used.

ASSOCIATED CONTENT

Supporting Information

The Supporting Information is available free of charge on the ACS Publications website. SEM images, XRD full width at half maximum, full in situ PL contour plots and low temperature PL

spectra of the $CH_3NH_3PbI_3$ films made with different antisolvent drip times and without antisolvent. Device performance and statistics

Author Contributions

C.M.S.-F. initiated this research. T.-B.S. and Z.Y. conducted the experiments. PLQY measurements were performed by D.P.N.. T.-B.S., Z.Y., F.B. and C.M.S.-F. evaluated the data. E.A. and S.D.W. synthesized and characterized photovoltaic devises. C.M.S.-F. directed the research and wrote the manuscript, all authors commented on the manuscript.

Corresponding Author

*E-mail:

Carolin M. Sutter-Fella: csutterfella@lbl.gov

Conflicts of interest

There are no conflicts of interest to declare.

Acknowledgements

This manuscript was prepared with support from the Laboratory Directed Research and Development (LDRD) program of Lawrence Berkeley National Laboratory under U.S. Department of Energy contract number DE-AC02-05CH11231(T.-B.S. and C.M.S.-F.). This material is based upon work performed by the Joint Center for Artificial Photosynthesis, a DOE Energy Innovation Hub, supported through the Office of Science of the U.S. Department of Energy under Award Number DE-SC0004993 (F.B.). D.P.N. gratefully acknowledges the National Science Foundation Graduate Research Fellowship under Grant DGE 1752814. E. A. and S. De W. thank King Abdullah University of Science and Technology (KAUST) for the award no. OSR-CARF URF/1/3079-33-01.

References

(1) Herz, L. M. Charge-Carrier Dynamics in Organic-Inorganic Metal Halide Perovskites. *Annu. Rev. Phys. Chem.* **2016**, *67*, 65–89.
(2) Brenner, T. M.; Egger, D. A.; Kronik, L.; Hodes, G.; Cahen, D. Hybrid Organic—Inorganic Perovskites: Low-Cost Semiconductors with Intriguing Charge-Transport Properties. *Nature Reviews Materials* **2016**, *1*, 15007.
(3) Stranks, S. D. Nonradiative Losses in Metal Halide Perovskites. *ACS Energy Lett.* **2017**, *2*, 1515–1525.
(4) Stoumpos, C. C.; Malliakas, C. D.; Kanatzidis, M. G. Semiconducting Tin and Lead Iodide Perovskites with Organic Cations: Phase Transitions, High Mobilities, and Near-Infrared Photoluminescent Properties. *Inorg. Chem.* **2013**, *52*, 9019–9038.
(5) NREL. Research Cell Efficiency Records: Https://Www.Nrel.Gov/Pv/.
(6) Stranks, S. D.; Snaith, H. J. Metal-Halide Perovskites for Photovoltaic and Light-Emitting Devices. *Nat Nano* **2015**, *10*, 391–402.
(7) Saliba, M.; Correa-Baena, J.-P.; Wolff, C. M.; Stolterfoht, M.; Phung, N.; Albrecht, S.; Neher, D.; Abate, A. How to Make over 20% Efficient Perovskite Solar Cells in Regular (n–i–p) and Inverted (p–i–n) Architectures. *Chem. Mater.* **2018**, *30*, 4193–4201.
(8) Paek, S.; Schouwink, P.; Athanasopoulou, E. N.; Cho, K. T.; Grancini, G.; Lee, Y.; Zhang, Y.; Stellacci, F.; Nazeeruddin, M. K.; Gao, P. From Nano- to Micrometer Scale: The Role of Antisolvent Treatment on High Performance Perovskite Solar Cells. *Chem. Mater.* **2017**, *29*, 3490–3498.
(9) Heo, J. H.; Song, D. H.; Im, S. H. Planar CH3NH3PbBr3 Hybrid Solar Cells with 10.4% Power Conversion Efficiency, Fabricated by Controlled Crystallization in the Spin-Coating Process. *Adv. Mater.* **2014**, *26*, 8179–8183.
(10) Tang, S.; Deng, Y.; Zheng, X.; Bai, Y.; Fang, Y.; Dong, Q.; Wei, H.; Huang, J. Composition Engineering in Doctor-Blading of Perovskite Solar Cells. *Adv. Energy Mater.* **2017**, *7*, 1700302.
(11) Hwang, K.; Jung, Y.-S.; Heo, Y.-J.; Scholes, F. H.; Watkins, S. E.; Subbiah, J.; Jones, D. J.; Kim, D.-Y.; Vak, D. Toward Large Scale Roll-to-Roll Production of Fully Printed Perovskite Solar Cells. *Adv. Mater.* **2015**, *27*, 1241–1247.
(12) Yang, M.; Li, Z.; Reese, M. O.; Reid, O. G.; Kim, D. H.; Siol, S.; Klein, T. R.; Yan, Y.; Berry, J. J.; van Hest, M. F. A. M.; Zhu, K. Perovskite Ink with Wide Processing Window for Scalable High-Efficiency Solar Cells. *Nature Energy* **2017**, *2*, 17038.
(13) Jeon, N. J.; Noh, J. H.; Kim, Y. C.; Yang, W. S.; Ryu, S.; Seok, S. I. Solvent Engineering for High-Performance Inorganic–Organic Hybrid Perovskite Solar Cells. *Nat Mater* **2014**, *13*, 897–903.
(14) Kojima, A.; Teshima, K.; Shirai, Y.; Miyasaka, T. Organometal Halide Perovskites as Visible-Light Sensitizers for Photovoltaic Cells. *J. Am. Chem. Soc.* **2009**, *131*, 6050–6051.
(15) Zhang, W.; Saliba, M.; Moore, D. T.; Pathak, S. K.; Hörantner, M. T.; Stergiopoulos, T.; Stranks, S. D.; Eperon, G. E.; Alexander-Webber, J. A.; Abate, A.; Sadhanala, A.; Yao, S.; Chen, Y.; Friend, R.H.; Estroff, L.A.; Wiesner, U.; Snaith, H.J. Ultrasmooth Organic–Inorganic Perovskite Thin-Film Formation and Crystallization for Efficient Planar Heterojunction Solar

Cells. *Nature Communications* **2015**, *6*, 6142.
(16) Eperon, G. E.; Burlakov, V. M.; Docampo, P.; Goriely, A.; Snaith, H. J. Morphological Control for High Performance, Solution-Processed Planar Heterojunction Perovskite Solar Cells. *Adv. Funct. Mater.* **2014**, *24*, 151–157.
(17) Burschka, J.; Pellet, N.; Moon, S.-J.; Humphry-Baker, R.; Gao, P.; Nazeeruddin, M. K.; Grätzel, M. Sequential Deposition as a Route to High-Performance Perovskite-Sensitized Solar Cells. *Nature* **2013**, *499*, 316–319.
(18) Bruening, K.; Tassone, C. J. Antisolvent Processing of Lead Halide Perovskite Thin Films Studied by in Situ X-Ray Diffraction. *J. Mater. Chem. A* **2018**, *6*, 18865–18870.
(19) Petrov, A. A.; Sokolova, I. P.; Belich, N. A.; Peters, G. S.; Dorovatovskii, P. V.; Zubavichus, Y. V.; Khrustalev, V. N.; Petrov, A. V.; Grätzel, M.; Goodilin, E. A.; Tarasov, A.B. Crystal Structure of DMF-Intermediate Phases Uncovers the Link Between CH3NH3PbI3 Morphology and Precursor Stoichiometry. *J. Phys. Chem. C* **2017**, *121*, 20739–20743.
(20) Rong, Y.; Tang, Z.; Zhao, Y.; Zhong, X.; Venkatesan, S.; Graham, H.; Patton, M.; Jing, Y.; Guloy, A. M.; Yao, Y. Solvent Engineering towards Controlled Grain Growth in Perovskite Planar Heterojunction Solar Cells. *Nanoscale* **2015**, *7*, 10595–10599.
(21) Jung, M.; Ji, S.-G.; Kim, G.; Seok, S. I. Perovskite Precursor Solution Chemistry: From Fundamentals to Photovoltaic Applications. *Chem. Soc. Rev.* **2019**, *48*, 2011–2038.
(22) Xiao, M.; Huang, F.; Huang, W.; Dkhissi, Y.; Zhu, Y.; Etheridge, J.; Gray-Weale, A.; Bach, U.; Cheng, Y.-B.; Spiccia, L. A Fast Deposition-Crystallization Procedure for Highly Efficient Lead Iodide Perovskite Thin-Film Solar Cells. *Angewandte Chemie* **2014**, *126*, 10056–10061.
(23) Li, J.; Yang, R.; Que, L.; Wang, Y.; Wang, F.; Wu, J.; Li, S. Optimization of Anti-Solvent Engineering toward High Performance Perovskite Solar Cells. *Journal of Materials Research* **2019**, *34*, 2416–2424.
(24) Xiao, M.; Zhao, L.; Geng, M.; Li, Y.; Dong, B.; Xu, Z.; Wan, L.; Li, W.; Wang, S. Selection of an Anti-Solvent for Efficient and Stable Cesium-Containing Triple Cation Planar Perovskite Solar Cells. *Nanoscale* **2018**, *10*, 12141–12148.
(25) Yavari, M.; Mazloum-Ardakani, M.; Gholipour, S.; Tavakoli, M. M.; Turren-Cruz, S.-H.; Taghavinia, N.; Grätzel, M.; Hagfeldt, A.; Saliba, M. Greener, Nonhalogenated Solvent Systems for Highly Efficient Perovskite Solar Cells. *Adv. Energy Mater.* **2018**, *8*, 1800177.
(26) Xin, D.; Wang, Z.; Zhang, M.; Zheng, X.; Qin, Y.; Zhu, J.; Zhang, W.-H. Green Anti-Solvent Processed Efficient Flexible Perovskite Solar Cells. *ACS Sustainable Chem. Eng.* **2019**, *7*, 4343–4350.
(27) Prochowicz, D.; Tavakoli, M. M.; Solanki, A.; Goh, T. W.; Pandey, K.; Sum, T. C.; Saliba, M.; Yadav, P. Understanding the Effect of Chlorobenzene and Isopropanol Anti-Solvent Treatments on the Recombination and Interfacial Charge Accumulation in Efficient Planar Perovskite Solar Cells. *J. Mater. Chem. A* **2018**, *6*, 14307–14314.
(28) Sakai, N.; Pathak, S.; Chen, H.-W.; Haghighirad, A. A.; Stranks, S. D.; Miyasaka, T.; Snaith, H. J. The Mechanism of Toluene-Assisted Crystallization of Organic–Inorganic Perovskites for Highly Efficient Solar Cells. *J. Mater. Chem. A* **2016**, *4*, 4464–4471.
(29) Zheng, X.; Chen, B.; Wu, C.; Priya, S. Room Temperature Fabrication of CH3NH3PbBr3 by Anti-Solvent Assisted Crystallization Approach for Perovskite Solar Cells with Fast Response and Small J–V Hysteresis. *Nano Energy* **2015**, *17*, 269–278.
(30) Cohen, B.-E.; Aharon, S.; Dymshits, A.; Etgar, L. Impact of Antisolvent Treatment on Carrier Density in Efficient Hole-Conductor-Free Perovskite-Based Solar Cells. *J. Phys. Chem.*

C **2016**, *120*, 142–147.
(31) Yang, F.; Kapil, G.; Zhang, P.; Hu, Z.; Kamarudin, M. A.; Ma, T.; Hayase, S. Dependence of Acetate-Based Antisolvents for High Humidity Fabrication of CH3NH3PbI3 Perovskite Devices in Ambient Atmosphere. *ACS Appl. Mater. Interfaces* **2018**, *10*, 16482–
(32) Wang, K.; Tang, M.-C.; Dang, H. X.; Munir, R.; Barrit, D.; Bastiani, M. D.; Aydin, E.; Smilgies, D.-M.; Wolf, S. D.; Amassian, A. Kinetic Stabilization of the Sol–Gel State in Perovskites Enables Facile Processing of High-Efficiency Solar Cells. *Adv. Mater.* **2019**, *31*,
(33) Poglitsch, A.; Weber, D. Dynamic Disorder in Methylammoniumtrihalogenoplumbates (II) Observed by Millimeter-wave Spectroscopy. *The Journal of Chemical Physics* **1987**, *87*, 6373–6378.
(34) Baikie, T.; Fang, Y.; Kadro, J. M.; Schreyer, M.; Wei, F.; Mhaisalkar, S. G.; Graetzel, M.; White, T. J. Synthesis and Crystal Chemistry of the Hybrid Perovskite (CH3NH3)PbI3 for Solid-State Sensitised Solar Cell Applications. *J. Mater. Chem. A* **2013**, *1*, 5628–5641.
(35) Song, T.-B.; Yuan, Z.; Mori, M.; Motiwala, F.; Segev, G.; Masquelier, E.; Stan, C. V.; Slack, J. L.; Tamura, N.; Sutter-Fella, C. M. Revealing the Dynamics of Hybrid Metal Halide Perovskite Formation via Multimodal In Situ Probes. *Adv. Funct. Mater. n/a* (n/a), 1908337. doi.org/10.1002/adfm.201908337.
(36) Guo, X.; McCleese, C.; Kolodziej, C.; Samia, A. C. S.; Zhao, Y.; Burda, C. Identification and Characterization of the Intermediate Phase in Hybrid Organic–Inorganic MAPbI3 Perovskite. *Dalton Trans.* **2016**, *45*, 3806–3813.
(37) Unold, T.; Gütay, L. Photoluminescence Analysis of Thin-Film Solar Cells. In *Advanced Characterization Techniques for Thin Film Solar Cells*; Abou-Ras, D., Kirchartz, T., Rau, U., Eds.; Wiley-VCH Verlag GmbH & Co. KGaA, 2011; pp 151–175.
(38) D'Innocenzo, V.; Srimath Kandada, A. R.; De Bastiani, M.; Gandini, M.; Petrozza, A. Tuning the Light Emission Properties by Band Gap Engineering in Hybrid Lead Halide Perovskite. *J. Am. Chem. Soc.* **2014**, *136*, 17730–17733.
(39) Nie, W.; Tsai, H.; Asadpour, R.; Blancon, J.-C.; Neukirch, A. J.; Gupta, G.; Crochet, J. J.; Chhowalla, M.; Tretiak, S.; Alam, M. A.; Wang, H.-L.; Mohite, A.D. High-Efficiency Solution-Processed Perovskite Solar Cells with Millimeter-Scale Grains. *Science* **2015**, *347*, 522–525.
(40) Wagner, L.; Mundt, L. E.; Mathiazhagan, G.; Mundus, M.; Schubert, M. C.; Mastroianni, S.; Würfel, U.; Hinsch, A.; Glunz, S. W. Distinguishing Crystallization Stages and Their Influence on Quantum Efficiency during Perovskite Solar Cell Formation in Real-Time. *Sci Rep* **2017**, *7*, 1–6.
(41) Akkerman, Q. A.; Motti, S. G.; Srimath Kandada, A. R.; Mosconi, E.; D'Innocenzo, V.; Bertoni, G.; Marras, S.; Kamino, B. A.; Miranda, L.; De Angelis, F.; Petrozza, A.; Prato, M.; Manna, L. Solution Synthesis Approach to Colloidal Cesium Lead Halide Perovskite Nanoplatelets with Monolayer-Level Thickness Control. *J. Am. Chem. Soc.* **2016**, *138*, 1010–1016.
(42) Hu, Q.; Zhao, L.; Wu, J.; Gao, K.; Luo, D.; Jiang, Y.; Zhang, Z.; Zhu, C.; Schaible, E.; Hexemer, A.; Wang, C.; Liu Y.; Zhang, W.; Grätzel, M.; Liu, F.; Russell, T.P.; Zhu, R.; Gong, Q. In Situ Dynamic Observations of Perovskite Crystallisation and Microstructure Evolution Intermediated from [PbI6]4− Cage Nanoparticles. *Nat. Commun.* **2017**, *8*, 15688.
(43) Sutter-Fella, C. M.; Li, Y.; Amani, M.; Ager, J. W.; Toma, F. M.; Yablonovitch, E.; Sharp, I. D.; Javey, A. High Photoluminescence Quantum Yield in Band Gap Tunable Bromide Containing Mixed Halide Perovskites. *Nano Lett.* **2016**, *16*, 800–806.
(44) Deschler, F.; Price, M.; Pathak, S.; Klintberg, L. E.; Jarausch, D.-D.; Higler, R.; Hüttner,

S.; Leijtens, T.; Stranks, S. D.; Snaith, H. J.; Atatüre, M.; Phillips R.T.; Friend, R.H. High Photoluminescence Efficiency and Optically Pumped Lasing in Solution-Processed Mixed Halide Perovskite Semiconductors. *J. Phys. Chem. Lett.* **2014**, *5*, 1421–1426.
(45) Ross, R. T. Some Thermodynamics of Photochemical Systems. *The Journal of Chemical Physics* **1967**, *46*, 4590–4593.
(46) Yablonovitch, E. Lead Halides Join the Top Optoelectronic League. *Science* **2016**, *351*, 1401–1401.
(47) Stolterfoht, M.; Caprioglio, P.; Wolff, C. M.; Márquez, J. A.; Nordmann, J.; Zhang, S.; Rothhardt, D.; Hörmann, U.; Amir, Y.; Redinger, A.; Kegelmann, L.; Zu, F.; Albrecht, S.; Koch, N.; Kirchartz, T.; Saliba, M.; Unold, T.; Neher, D. The Impact of Energy Alignment and Interfacial Recombination on the Internal and External Open-Circuit Voltage of Perovskite Solar Cells. *Energy Environ. Sci.* **2019**, *12*, 2778–2788.
(48) D'Innocenzo, V.; Grancini, G.; Alcocer, M. J. P.; Kandada, A. R. S.; Stranks, S. D.; Lee, M. M.; Lanzani, G.; Snaith, H. J.; Petrozza, A. Excitons versus Free Charges in Organo-Lead Tri-Halide Perovskites. *Nat Commun* **2014**, *5*, 3586.
(49) Galkowski, K.; Mitioglu, A. A.; Surrente, A.; Yang, Z.; Maude, D. K.; Kossacki, P.; Eperon, G. E.; Wang, J. T.-W.; Snaith, H. J.; Plochocka, P.; Nicholas, R.J. Spatially Resolved Studies of the Phases and Morphology of Methylammonium and Formamidinium Lead Tri-Halide Perovskites. *Nanoscale* **2017**, *9*, 3222–3230.
(50) Wehrenfennig, C.; Liu, M.; Snaith, H. J.; Johnston, M. B.; Herz, L. M. Charge Carrier Recombination Channels in the Low-Temperature Phase of Organic-Inorganic Lead Halide Perovskite Thin Films. *APL Materials* **2014**, *2*, 081513.
(51) Wu, X.; Trinh, M. T.; Niesner, D.; Zhu, H.; Norman, Z.; Owen, J. S.; Yaffe, O.; Kudisch, B. J.; Zhu, X.-Y. Trap States in Lead Iodide Perovskites. *J. Am. Chem. Soc.* **2015**, *137*, 2089–2096.
(52) Aydin, E.; Bastiani, M. D.; Wolf, S. D. Defect and Contact Passivation for Perovskite Solar Cells. *Advanced Materials* **2019**, *31*, 1900428.
(53) Zhou, H.; Chen, Q.; Li, G.; Luo, S.; Song, T.; Duan, H.-S.; Hong, Z.; You, J.; Liu, Y.; Yang, Y. Interface Engineering of Highly Efficient Perovskite Solar Cells. *Science* **2014**, *345*, 542–546.
(54) Bronstein, N. D.; Yao, Y.; Xu, L.; O'Brien, E.; Powers, A. S.; Ferry, V. E.; Alivisatos, A. P.; Nuzzo, R. G. Quantum Dot Luminescent Concentrator Cavity Exhibiting 30-Fold Concentration. *ACS Photonics* **2015**, *2*, 1576–1583.
(55) Aydin, E.; Troughton, J.; De Bastiani, M.; Ugur, E.; Sajjad, M.; Alzahrani, A.; Neophytou, M.; Schwingenschlögl, U.; Laquai, F.; Baran, D.; Wolf, S.D. Room-Temperature-Sputtered Nanocrystalline Nickel Oxide as Hole Transport Layer for p–i–n Perovskite Solar Cells. *ACS Appl. Energy Mater.* **2018**, *1*, 6227–6233.